Supporting Information

Angstrom-Scale-Distance Dependent Synergy in Cluster via Atom-by-Atom Regulation for Enhanced Photocatalytic CO_2 Reduction

Haijiao Yin,[a#] Yuting Luo,[b#] Rui Lu,[a#] En Guo,[a] Yuanxin Du,[a*] Pu Wang,[b*] Manzhou Zhu[a*]

[a] Department of Materials Science and Engineering, Centre for Atomic Engineering of Advanced Materials, Key Laboratory of Structure and Functional Regulation of Hybrid Materials of Ministry of Education, Key Laboratory of Functional Inorganic Material Chemistry of Anhui Province, Anhui University, Hefei 230601, China

[b] Department of Chemistry, Key Laboratory of Environmentally Friendly Chemistry and Applications of Ministry of Education, Xiangtan University, Xiangtan, Hunan 411105, China

[#] These authors contributed equally to this work.

* Corresponding author. E-mail: duyuanxin@ahu.edu.cn, 90wangpu@xtu.edu.cn, zmz@ahu.edu.cn

1.1 Experimental section

Materials: palladium chloride ($PdCl_2$, 99%), hydrochloric acid (AR), palladium acetate ($Pd(CH_3COO)_2$, 99%), palladium nitrate dihydrate ($Pd(NO_3)_2 \cdot 2H_2O$, 99.99%), triphenylphosphine (PPh_3, 99%), palladium(II)bis(triphenylphosphine) dichloride ($Pd(PPh_3)_2Cl_2$, 99%), sodium borohydride ($NaBH_4$, 99.99%), tetraphenylphosphonium bromide (PPh_4Br, 98%), titanium dioxide (TiO_2, 99%), methylene chloride (CH_2Cl_2, HPLC grade), triethylamine (AR), phenylethyl mercaptan (99%), tetrahydrofuran (THF, HPLC grade), acetic ether ($CH_3COOC_2H_5$, HPLC grade), methanol (CH_3OH, HPLC grade), acetonitrile (CH_3CN, HPLC grade), n-hexane (Hex, HPLC grade), 2,4-dimethylthiophenol (2,4-DMBTH, 99%), and ethanol were bought from Sigma–Aldrich or Aladdin Reagent. Ultrapure deionized water (18.2 MΩ cm^{-1}) was used in all experiments. All of the above chemicals were used as received without further purification. All glassware was thoroughly cleaned with aqua regia (HCl : HNO_3 = 3 : 1 vol%), rinsed with copious pure water, and then dried in an oven prior to use.

Synthesis of TiO_2: 200 mg purchased TiO_2 powder and 30 mg $NaBH_4$ were evenly mixed in a mortar, transferred to a porcelain boat and calcined at 350 ℃ for 30 min. After calcination, the material was cleaned with water and ethanol three times.

Synthesis of Pd_2: Pd_2 was prepared according to a previously reported method with some modifications. $Pd(CH_3COO)_2$ (50.0 mg, 0.223 mmol) and PPh_3 (100.0 mg, 0.381 mmol) were dissolved in 10 mL THF and the mixture was stirred continuously in the flask for 5 min. Then, 2, 4-DMBTH (120.0 mg, 0.868 mmol) was added. After two minutes, a cold aqueous solution of sodium borohydride (130.0 mg, 3.44 mmol) was added. After 5 minutes, the reaction completed, the black solution was washed with methanol. The Pd_2 was isolated from the crude product by preparative thin layer chromatography (PTLC).

Synthesis of Pd_3: Pd_3 was prepared according to a previously reported method with some modifications. 1.42 g $PdCl_2$ was added to 10 mL hydrochloric acid, then 0.6 mL (0.48 mmol) of the above solution was added into 10 mL THF. Triphenylphosphine (0.313 g, 1.2 mmol) was added, and the mixture was stirred intensely for 8 minutes. Next, 5 mL of an ethanolic $NaBH_4$ (1.6 mg/mL) solution was added and the solution was stirred vigorously for 1 h. The undissolved (excessive) triphenylphosphine was removed by centrifugation. The remaining solution was dried by vacuum evaporation using a rotary distillation machine. The product was washed with water and methylene chloride, then evaporated again until dry. The product Pd_3 was obtained by adding excess n-hexane, followed by precipitation and centrifugation.

Synthesis of Pd_5: Pd_5 was prepared according to a previously reported method with some modifications. $Pd(NO_3)_2{\cdot}2H_2O$ (135 mg, 0.51 mmol), phenylethyl mercaptan (150 μL, 1.1 mmol), and triethylamine (150 μL, 1.08 mmol) were dissolved in 6 mL acetonitrile, and the mixture was stirred rapidly. The reaction was stopped after 5 h. The yellow precipitate obtained was washed with excess deionized water and ethanol. The mixed precipitate was extracted with methylene chloride, centrifuged to remove the undissolved product, and then separated by PTLC using a mixture of methylene chloride and petroleum ether (1/2 v : v) to obtain Pd_5.

Synthesis of Pd_x-TiO_2: 4 mg Pd_x was dissolved in dichloromethane, and 100 mg TiO_2 dispersed in ethanol was added into the flask. The mixture was homogenized by stirred thoroughly, and the dried

by rotary evaporation apparatus to obtain the Pd_x-TiO_2.

Synthesis of Pd NP-TiO_2: 6.7 mg of $PdCl_2$ was weighed, dissolved in deionized water, and a small amount of dilute hydrochloric acid was added. After $PdCl_2$ was completely dissolved, 100 mg of TiO_2 was added. The mixture was stirred and ultrasonicated to ensure uniform dispersion. Then, a $NaBH_4$ solution was slowly added under stirring. The precipitate was collected by centrifugation, washed with deionized water and ethanol, and dried in a vacuum oven to obtain 4 wt% Pd NP-TiO_2.

1.2 Material characterization

TEM image was recorded using a transmission electron microscope (JEM ARM-200F, JEOL). XRD pattern was collected on diffractometer (Smart Lab 9 kW, Japan) with Cu Kα radiation (λ= 0.15418 nm). XPS spectrum was performed on Esca Lab 250Xi X-ray Photoelectron Spectrometer. UV-vis diffuse reflectance spectroscopy (DRS) was conducted on Hitachi U-3900 UV-visible spectrophotometer with barium sulfate as a reference. CO_2 adsorption was measured on automatic microporous gas adsorption analyzer ASAP 2020. Photoluminescence (PL) emission spectrum and lifetime were obtained by using fluorescence spectrophotometer (Hitachi, F-4600) and ultra-fast time-resolved fluorescence spectrometer (Horiba Fluoro max plus), respectively. Thermo Fisher Scientific TSQ8000EVO gas chromatography-mass spectrometry (GC-MS) was used to detect ^{13}C and ^{12}C labeled products. Photoelectrochemical tests were conducted on an electrochemical workstation (CHI 760E, Chen Hua Instrument, China). The glassy carbon (indium-doped tin oxide for photocurrent test), Pt foil, and Ag/AgCl (saturated KCl) were acted as working, counter, and reference electrode, respectively. Na_2SO_4 (0.5 M, pH = 7) was as electrolyte.

1.3 In situ attenuated total reflectance Fourier transform infrared spectroscopy (ATR-FTIR) measurement

In situ ATR-FTIR spectra were obtained by using a temperature-controlled Perkin Elmer instrument. The catalyst was evenly applied to the silicon single crystal and placed on the optical attachment. High purity CO_2 was injected into the reaction tank and bubbled for 30 minutes. Turned on the xenon lamp and collected signals at ten-minute intervals. The machine was equipped with a liquid nitrogen-cooled MCT detector and PIKE Vee MAX optical attachment.

1.4 The calculation of apparent quantum yield (AQY)

Considering the photocatalytic CO_2 reduction process in this system involves the following two types of reactions:

$$CO_2 + 2H^+ + 2e^- \rightarrow CO + H_2O \quad (1)$$

$$CO_2 + 8H^+ + 8e^- \rightarrow CH_4 + 2H_2O \quad (2)$$

The apparent quantum yield (AQY) can be calculated by the following equation:

$$\text{AQY}\,(\%) = \frac{\text{Ne}}{\text{N}_\text{p}} \times 100\% = \frac{(M_{CO} \times 2 + M_{\text{CH4}} \times 8) \times N_A \times \text{h} \times \text{c}}{P \times S \times t \times \lambda} \times 100\% \quad (3)$$

Ne and Np represent the number of electrons required for the reaction product and the number of incident photons, respectively. M_{CO} and M_{CH4} represent the Molar amount of generated CO and CH_4, respectively. N_A, P, S, t, λ, h, c are the Avogadro constant (6.02×10^{23} mol^{-1}), the light intensity (100 mW/cm^2), the irradiated area (9.07 cm^2), the exposure time, the wavelength of the incident light (420 nm), the Planck's constant (6.62×10^{-34} J·s), the speed of light (3×10^8 $m\cdot s^{-1}$), respectively.

1.5 The calculation of yield

$$\text{Yield} = \frac{n_{product}}{m_{cat} \times t} \quad (4)$$

$n_{product}$: the amount of product in moles (μmol).

m_{cat}: mass of the catalyst (g).

t: reaction time (h).

1.6 Computational method

All geometry optimizations for each catalytic intermediate were performed using density functional theory (DFT) as implemented in the DMol^3 program in the Materials Studio package.[1,2] Due to computational cost and time factors, the real ligands of all clusters are simplified to methyl. The generalized gradient approximation (GGA) with the Perdew-Burkr-Ernzerhof (PBE) functional,[3,4] the double-ζ numerical basis set with polarization d-function (DND) and semi-core pseudopotential (DSPP) approximation were adopted.[5] The Tkatchenko-Scheffler (TS) method was used for the dispersion correction.[6] The real-space global cutoff radius is set to be 4.5 angstrom. The

convergence criterion of the geometrical optimization was set to be 1.0×10^{-5} Hartree for energy change, 4.0×10^{-3} Hartree/Å for the gradient, and 5.0×10^{-3} Å for the atom displacement, respectively. The analysis of chemical bond formation and properties was conducted using the Atoms in Molecules (AIM) theory via the Multiwfn software.[7] The input files were generated by Gaussian 16.[8] For single-point energy calculations, the PBE functional was employed, with the 6-31g** basis set for C, H, Cl, and P atoms, and the LANL2dz basis set for Pd atoms.

This paper constructs a three-layer TiO_2 substrate model to simulate, considering the adsorption of various Pd nanoclusters on the TiO_2 surface. Atoms in the bottom two layers were fixed at their lattice positions, and all other atoms including adsorbates were allowed to relax. A vacuum layer about 20 Å thickness was added to the slab to ensure that there were no interactions between the slab and the periodic structures perpendicular to the surface.

The Gibbs free energy of CO adsorption (ΔG_{ad}) was calculated according to $\Delta G_{ad} = G_{CO*} - G_{*} - G_{CO}$, where G_{CO*}, G_{*}, and G_{CO} represent the total Gibbs free energies of the catalyst slab with adsorbed CO, the corresponding catalyst slab, and the free CO molecule, respectively. A positiveΔG_{ad} indicates an endothermic adsorption process, whereas a negative ΔG_{ad} corresponds to an exothermic process. The calculated ΔG_{ad} values are summarized in **Table S5**.

The reaction free energies of the photocatalytic steps were calculated using the computational hydrogen electrode proposed by Nørskov et al, where the chemical potential of proton-electron pair ($H^+ + e^-$) is equal to a half of the chemical potential of the gas phase H_2.[9]

The reaction pathways of the CO_2 reduction reaction (CO_2RR, $CO_2 + 2H^+ + 2e^- \rightarrow CO + H_2O$) can be written as:

$$*+ CO_2 + H^+ + e^- \rightarrow COOH^* \quad (1)$$

$$COOH^* + H^+ + e^- \rightarrow CO^* + H_2O \quad (2)$$

$$CO^* \rightarrow *+ CO \quad (3)$$

where * denotes the active site of the catalyst. The Gibbs free energy change (ΔG) for the elementary reaction was calculated by following equations:

$$\Delta G_1 = G(COOH^*) - G(^*) - G(CO_2) - {}^1\!/_2 G(H_2) \quad (4)$$

$$\Delta G_2 = G(CO^*) + G(H_2O) - G(COOH^*) - {}^1\!/_2 G(H_2) \quad (5)$$

$$\Delta G_3 = G(^*) + G(CO) - G(CO^*) \quad (6)$$

The species Gibbs free energy was determined by $\Delta G = \Delta E + \Delta ZPE - T\Delta S$,[10] where ΔE is the change of reaction energy directly obtained from the DFT total energies, ΔZPE is the change of zero-point energy, T is the system temperature of 298.15 K, and ΔS is the change in entropy.[11,12] Zero-point energies and entropies were computed from the vibrational frequencies. For the adsorption of intermediates COOH*, CO* and H*, vibrational frequency evaluation for surface adsorbates considered the 3N degrees of freedom of the adsorbates. The $\Delta ZPE - T\Delta S$ for adsorbed species and gas phase species are presented in **Table S6**.

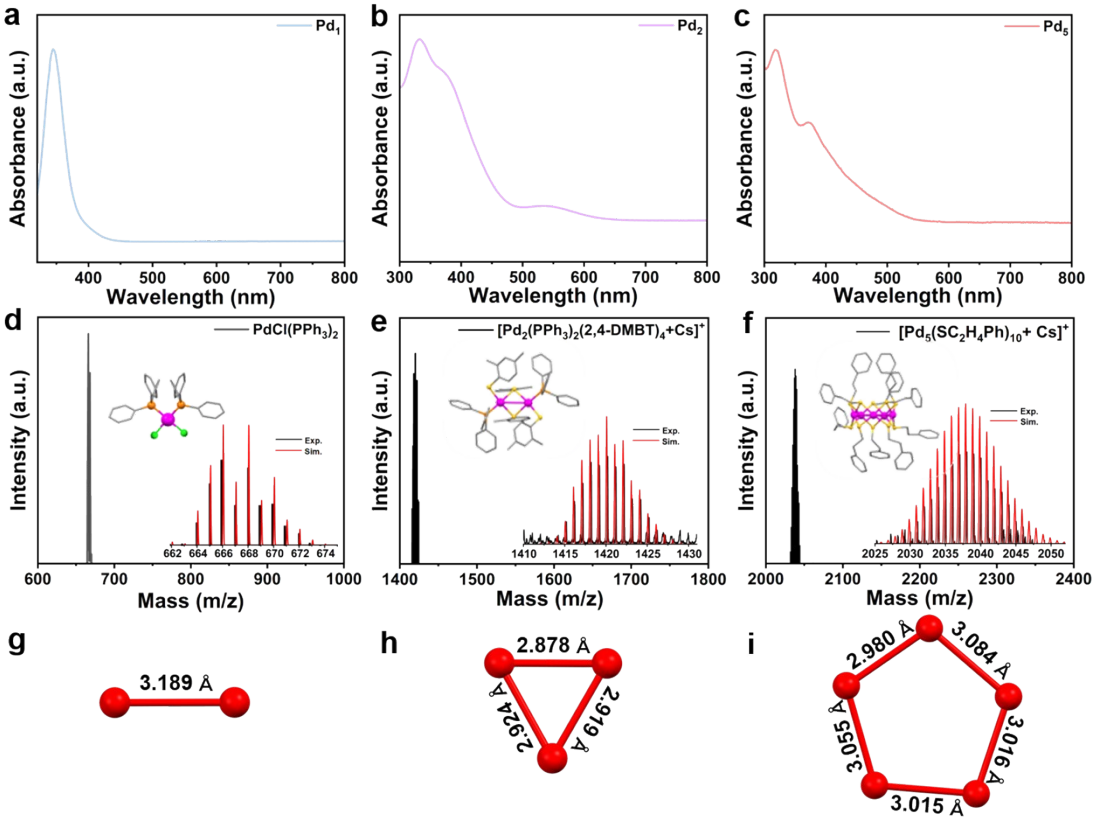

Figure S1. (a-c) UV-vis absorbance spectra of Pd_x (x = 1, 2 and 5). (d-f) Positive-ion mode ESI-MS spectra and corresponding crystal structure of Pd_x (x = 1, 2 and 5) Color codes: Pd = magenta, P = orange, S = yellow, Cl = green, C = gray. (g-i) The Pd-Pd bond length of Pd_x (x = 1, 2 and 5).

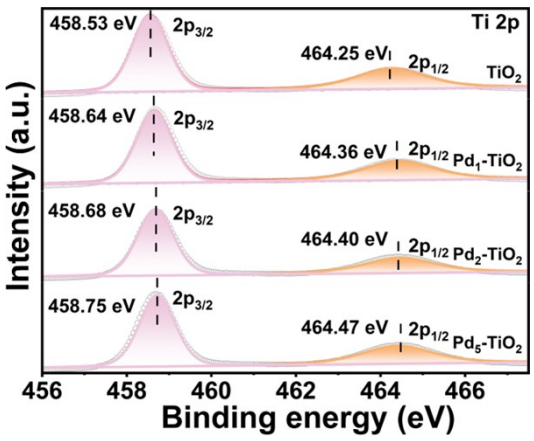

Figure S2. Ti 2p XPS spectra of TiO_2 and Pd_x-TiO_2 (x = 1, 2 and 5).

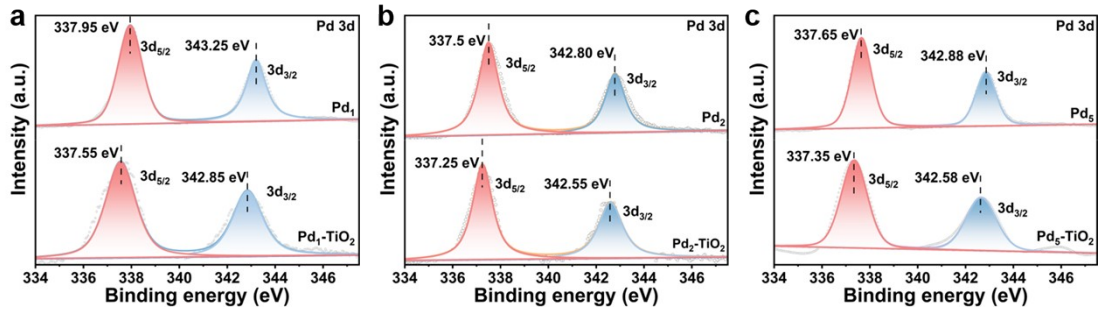

Figure S3. (a-c) Pd 3d XPS spectra of Pd_x and Pd_x-TiO_2 (x = 1, 2 and 5).

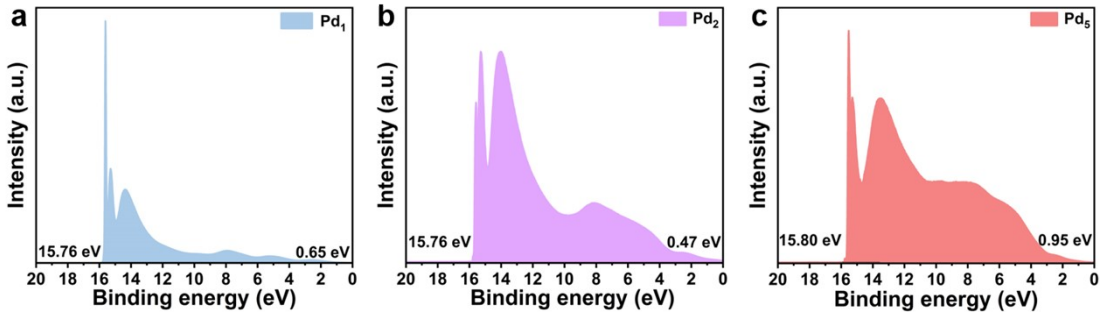

Figure S4. UPS spectra of (a) Pd_1, (b) Pd_2 and (c) Pd_5.

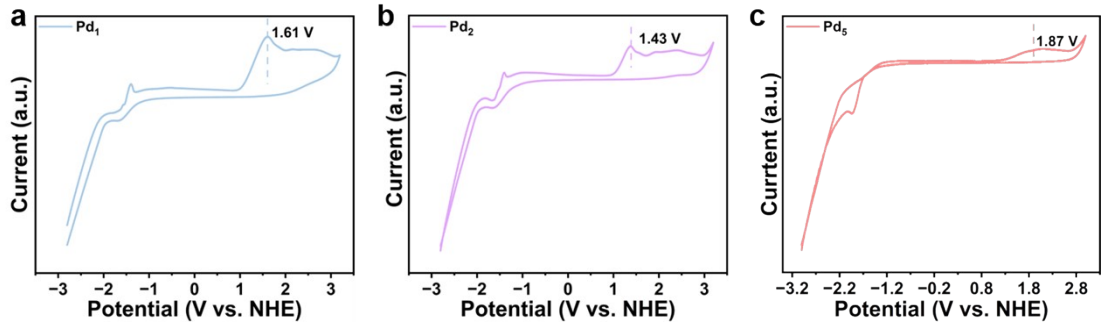

Figure S5. CV curves of (a) Pd_1, (b) Pd_2 and (c) Pd_5.

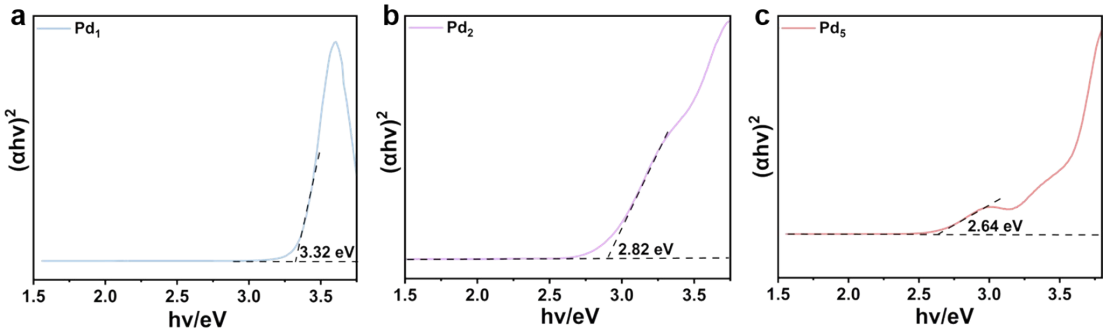

Figure S6. Tauc plots of (a) Pd_1, (b) Pd_2 and (c) Pd_5.

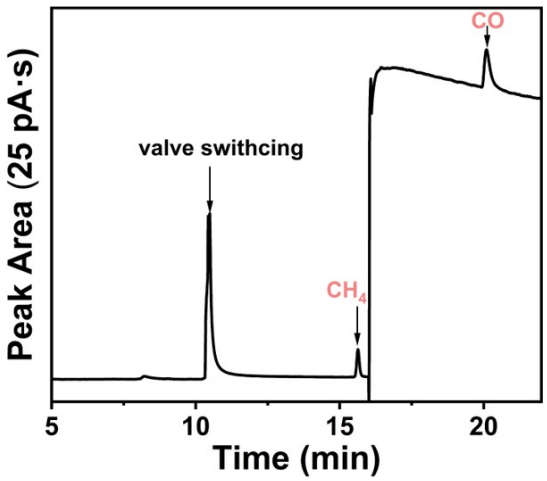

Figure S7. The on-line GC spectrum of gas product detected on FID detector.

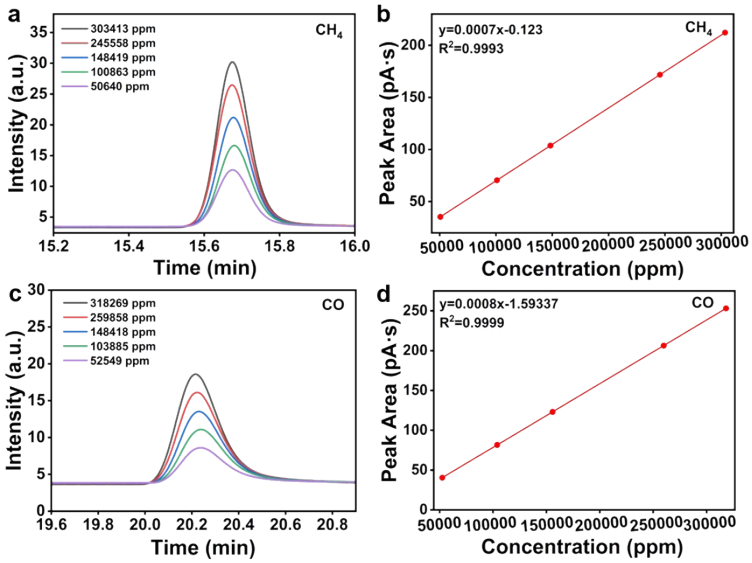

Figure S8. (a) GC spectra of different CH_4 content. (b) The corresponding concentration-peak area calibration curve of CH_4. (c) GC spectra of different CO content. (d) The corresponding concentration-peak area calibration curve of CO.

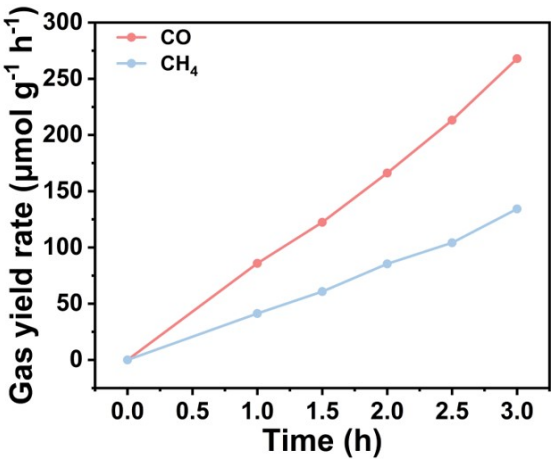

Figure S9. Time-dependent photocatalytic CO and CH_4 production of Pd_3-TiO_2.

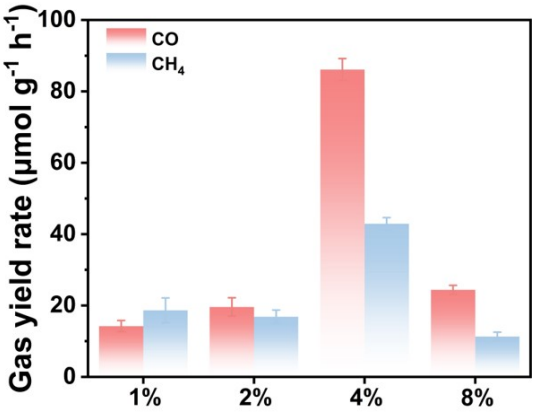

Figure S10. Photocatalytic CO and CH_4 production rate of Pd_3-TiO_2 with different contents of Pd_3.

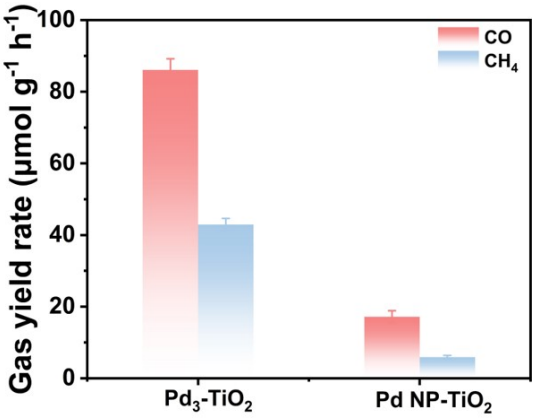

Figure S11. The comparison of photocatalytic CO and CH_4 production rate of Pd_3-TiO_2 and Pd NP-TiO_2.

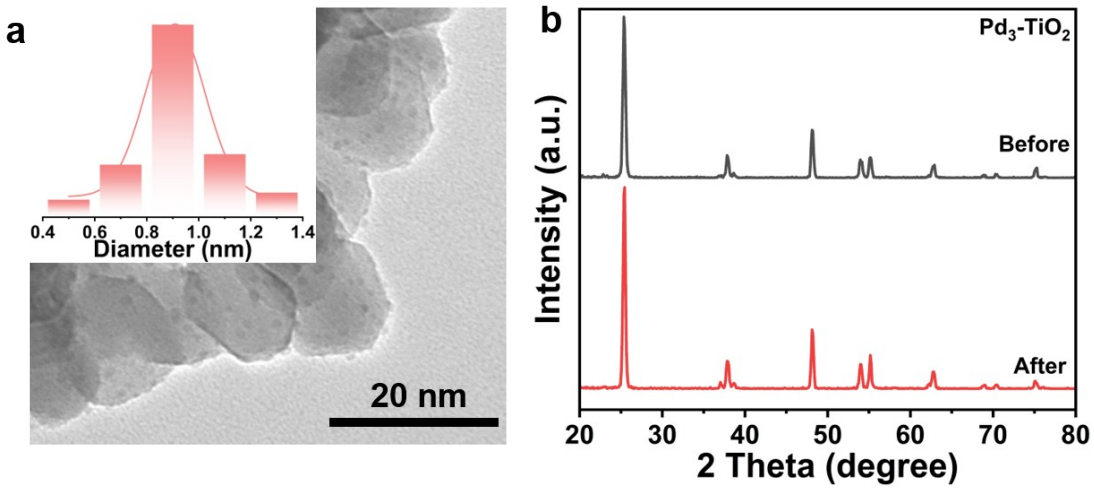

Figure S12. (a) TEM image and (b) XRD pattern of Pd_3-TiO_2 after reaction.

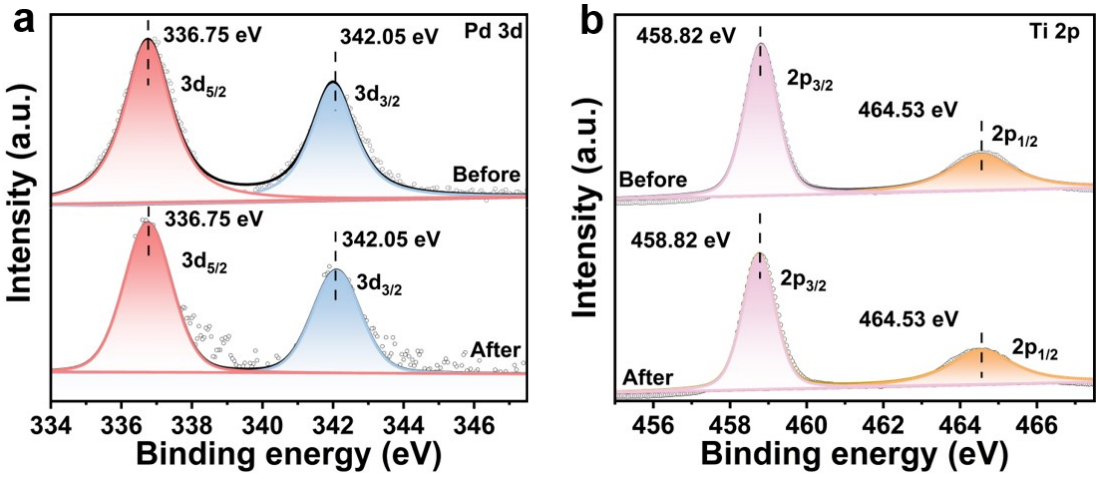

Figure S13. (a) Pd 3d and (b) Ti 2p XPS spectra of Pd_3-TiO_2 before and after photocatalytic CO_2 reduction.

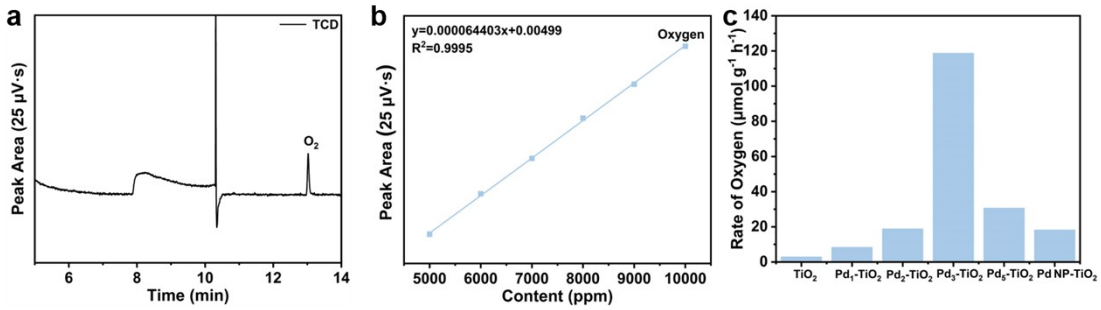

Figure S14. (a) The GC spectrum of O_2 detected on TCD and (b) the corresponding fitting calibration curve. (c) The O_2 production rate of different samples.

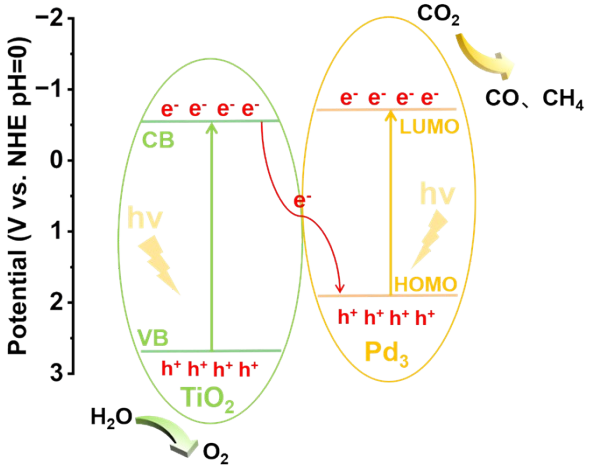

Figure S15. Schematic illustration of Z-scheme charge transfer pathway in Pd_3-TiO_2 heterojunction during photocatalytic CO_2RR.

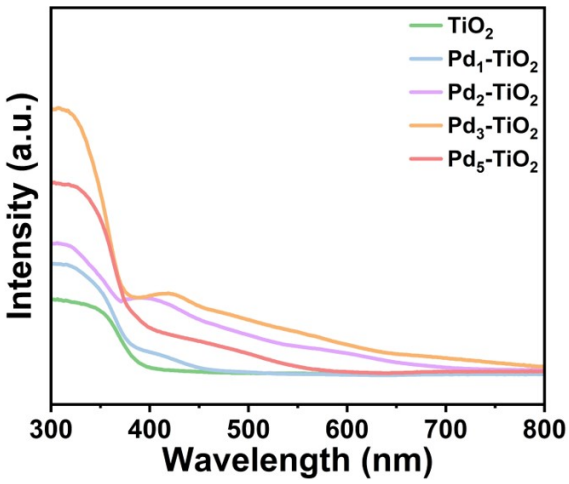

Figure S16. UV-vis diffuse reflection spectroscopy of different samples.

(a) $Pd_2(P(CH_3)_3)_2(SCH_3)_4$

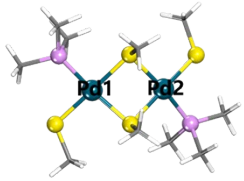

Bond	Length/Å	ρ(r)/a.u.
Pd1-Pd2	3.410	-

(b) $Pd_3Cl(P(CH_3)_2)_2(P(CH_3)_3)_3^+$

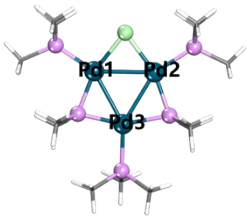

Bond	Length/Å	ρ(r)/a.u.
Pd1-Pd2	2.959	0.0178
Pd2-Pd3	2.968	-
Pd1-Pd3	2.957	-

(c) $Pd_5(SC_2H_5)_{10}$

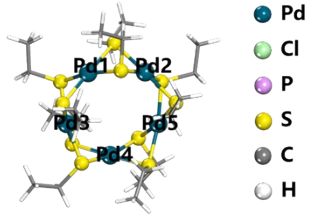

Bond	Length/Å	ρ(r)/a.u.
Pd1-Pd2	3.078	-
Pd1-Pd3	3.137	-
Pd3-Pd4	3.051	-
Pd4-Pd5	3.100	-
Pd2-Pd5	3.114	-

Figure S17. Pd-Pd bond lengths and electron densities at bond critical points (BCPs) in Pd clusters.

"-" indicates a weak interaction with no available electron density data.

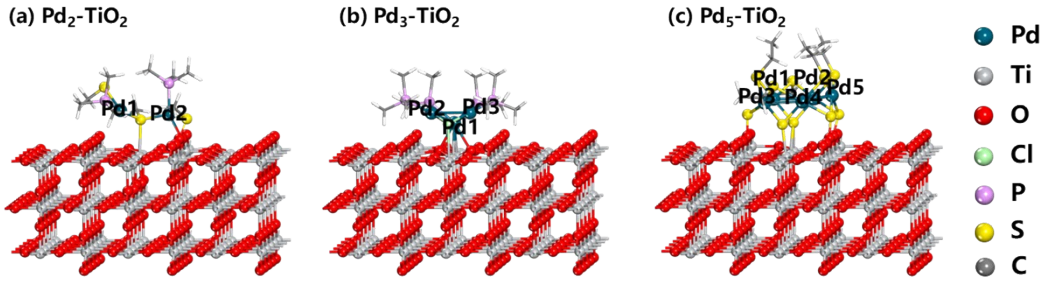

	Length (Å)
Pd1-Pd2	3.677

	Length (Å)
Pd1-Pd2	2.957
Pd2-Pd3	2.847
Pd1-Pd3	2.958

	Length (Å)
Pd1-Pd2	3.040
Pd1-Pd3	3.285
Pd3-Pd4	2.800
Pd4-Pd5	2.977
Pd2-Pd5	2.935

Figure S18. Pd-Pd bond lengths in Pd_x-TiO_2 (x = 2, 3, and 5).

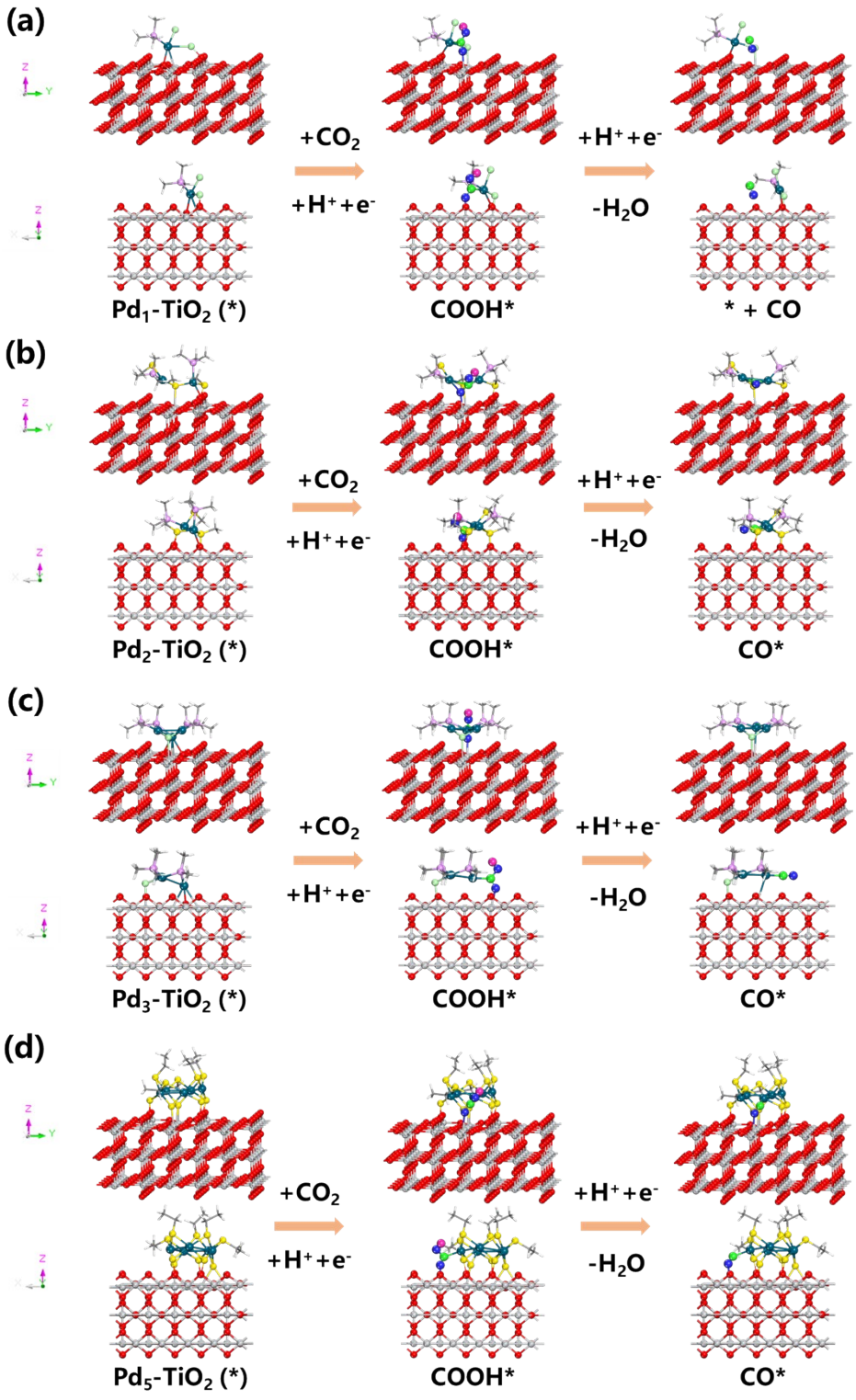

Figure S19. Structural schematic diagram of reactants, intermediates, and products along the photocatalytic CO_2RR reaction pathway on (a) Pd_1-TiO_2, (b) Pd_2-TiO_2, (c) Pd_3-TiO_2, and (d) Pd_5-TiO_2.

Table S1. The CO and CH_4 production rate of different samples.

Photocatalysts	CO (μmol g^{-1} h^{-1})	CH_4 (μmol g^{-1} h^{-1})
TiO_2	4.26	0.82
Pd_1-TiO_2	5.21	3.59
Pd_2-TiO_2	19.76	5.98
Pd_3-TiO_2	86.09	42.94
Pd_5-TiO_2	29.13	9.98
Pd NP-TiO_2	17.20	5.94

Table S2. The performance comparison of photocatalytic CO_2 reduction to CO/CH_4 in various samples.

Catalyst	Light source	Condition	Products and yields/μmol $gcat^{-1}$ h^{-1}	AQY/%	References
Pd-HPP-TiO_2	300 W Xe lamp	CO_2 and water	CO 34 CH_4 48	/	Nat. Commun. 2022, 13, 1400
Cu-TiO_2	300 W Xe lamp	CO_2 and water	CO 15.27	/	Angew. Chem. Int. Ed. 2022, 61, e202207600
Pd/PdSA/TiO_2	300 W Xe lamp	CO_2 and water	CH_4 37.28	/	Adv. Funct. Mater. 2025, e22529
Mn-Co_3O_4	300 W Xe lamp	CO_2 and water	CH_4 23.4	/	J. Am. Chem. Soc. 2024, 146, 15338
$Cs_2AgBiBr_6$	AM 1.5	CO_2 and water	CO 14.1 CH_4 9.6	/	Adv. Sci. 2024, 11, 2309526
PW_9/g-C_3N_4	300 W Xe lamp	CO_2 and water	CH_4 40.8	3.01% 380 nm	Angew. Chem. Int. Ed. 2025, 64, e202413594
Pd_{TP}/Pd_{SA}-CN	300 W Xe lamp	CO_2 and water	CH_4 46.5	/	Adv. Power Mater. 2024, 3, 100170
Cu_1-TiO_2/$BiVO_4$	300 W Xe lamp	CO_2 and water	CO 17.33	/	J. Am. Chem. Soc. 2024, 146, 9163
BTOPAu	300 W Xe lamp	CO_2 and water	CO 34.15	/	Nat. Commun. 2024, 15, 305
Al-Au-0.5	300 W Xe lamp	CO_2 and water	CO 31.7	/	Appl. Catal. B. Environ. 2024, 345, 123703
44BP-TiO_2	300 W Xe lamp	CO_2 and water	CH_4 10.76	/	J. Am. Chem. Soc. 2023, 145, 5769
Ni_1/P-CN	300 W Xe lamp	CO_2, MeCN, BIH, TFE	CO 71	0.32% 400 nm	Carbon Energy. 2024, 6, 533
Cu_3-BPY-COF(Ru/CO)-2	visible light λ > 420 nm	CO_2, MeCN, H_2O	CH_4 31.5	/	Angew. Chem. Int. Ed. 2025, 64, e202505546
Cu SAs /TiO_2	300 W Xe lamp	CO_2 and water	CO 65.8	2% 420 nm	ACS Catal. 2022, 12, 14096
C-ZnO-500	300 W Xe lamp	CO_2 and water	CO 30.09	/	Appl. Catal. B. Environ. 2026, 383, 126025
Pd_1+NPs/C_3N_4	300 W Xe lamp	CO_2 and water	CH_4 20.3	2.93% 385 nm	Adv. Mater. 2022, 34, 2200057
PAN-332-DCM	300 W Xe lamp	CO_2 and water	CO 74.7	0.13% 808 nm	Angew. Chem. Int. Ed. 2025, 64, e202508924
Cu NCs/TiO_2	300 W Xe lamp	CO_2 and water	CH_4 40.3	/	Chem. Eng. J. 2022, 445, 136718
TBHO	365 nm LED	CO_2 and water	CO 29.1	/	Adv. Funct. Mater. 2024, 34, 2311663

$TiZrNbTaZnO_{10}$	400W Hg lamp	CO_2 and water	CO 25.3 CH_4 9.99	/	Appl. Catal. B. Environ. 2025, 371, 125259
Pd_3-TiO_2	300 W Xe lamp	CO_2 and water	CO 86.09 CH_4 42.94	4.49% 420 nm	This work

Table S3. The actual O_2 production rate and theoretical production rate of different samples.

Photocatalysts	Oxygen (μmol g^{-1} h^{-1})	Theoretical Oxygen (μmol g^{-1} h^{-1})
TiO_2	2.88	3.77
Pd_1-TiO_2	8.36	9.785
Pd_2-TiO_2	18.86	21.84
Pd_3-TiO_2	118.68	128.925
Pd_5-TiO_2	30.65	34.525
Pd NP-TiO_2	18.23	20.48

Table S4. Charge distribution of Pd_x and Pd_x-TiO_2 (x = 1, 2, 3 and 5).

Charge (e)		Pd_x	Pd_x-TiO_2	Δ (e)
x = 1	Pd1	0.054	-0.105	-0.159
x = 2	Pd1	-0.177	-0.359	-0.182
	Pd2	-0.227	-0.300	-0.073
	sum	-0.404	-0.659	-0.255
x = 3	Pd1	-0.238	-0.295	-0.057
	Pd2	-0.278	-0.425	-0.147
	Pd3	-0.264	-0.404	-0.140
	sum	-0.780	-1.124	-0.344
x = 5	Pd1	-0.151	-0.231	-0.080
	Pd2	-0.162	-0.241	-0.079
	Pd3	-0.191	-0.185	-0.006
	Pd4	-0.185	-0.246	-0.061
	Pd5	-0.194	-0.240	-0.046
	sum	-0.883	-1.143	-0.260

Table S5. Calculated Gibbs free energies for CO adsorption on Pd_x-TiO_2 (x = 1, 2, 3 and 5).

	ΔG_{ad} (eV)
Pd_1-TiO_2	-
Pd_2-TiO_2	0.08
Pd_3-TiO_2	-0.53
Pd_5-TiO_2	0.38

Table S6. The ZPE and TS for adsorbed species and gas phase species.

species	ZPE-TS (eV)
H_2	-0.22
CO	-0.81
CO_2	0.09
H_2O	0.12
Pd_1-TiO_2-COOH	0.45
Pd_2-TiO_2-COOH	0.51
Pd_2-TiO_2-CO	0.16
Pd_3-TiO_2-COOH	0.49
Pd_3-TiO_2-CO	0.07
Pd_5-TiO_2-COOH	0.49
Pd_5-TiO_2-CO	0.11

References

[1] Botti, S. Applications of Time-Dependent Density Functional Theory. Phys. Scr. 2004, T109, 54−60.

[2] Adamo C, Jacquemin D. The calculations of excited-state properties with Time-Dependent Density Functional Theory. Chemical Society Reviews, 2013, 42(3): 845-856.

[3] Kresse, G.; Joubert, D. From ultrasoft pseudopotentials to the projector augmented-wave method. Phys. Rev. B: Condens. Matter Mater. Phys. 1999, 59, 1758−1775.

[4] Perdew, J. P.; Burke, K.; Ernzerhof, M. Generalized gradient approximation made simple. Phys. Rev. Lett. 1996, 77, 3865−3868.

[5] Hamann D R, Schlüter M, Chiang C. Norm-conserving pseudopotentials. Physical Review Letters, 1979, 43(20): 1494.

[6] Tkatchenko A, Scheffler M. Accurate molecular van der Waals interactions from ground-state electron density and free-atom reference data. Physical review letters, 2009, 102(7): 073005.

[7] Lu T., Chen F. Multiwfn: A multifunctional wavefunction analyzer[J]. Journal of Computational Chemistry, 2012, 33(5): 580-592.

[8] Frisch M. J., Trucks G. W., Schlegel H. B., et al. Gaussian 16, gaussian[J]. Inc., Wallingford CT, 2016, 2016.

[9] Nørskov J K, Rossmeisl J, Logadottir A, et al. Origin of the overpotential for oxygen reduction at a fuel-cell cathode. The Journal of Physical Chemistry B, 2004, 108(46): 17886-17892.

[10] Nitopi S, Bertheussen E, Scott S B, et al. Progress and perspectives of electrochemical CO_2 reduction on copper in aqueous electrolyte. Chemical reviews, 2019, 119(12): 7610-7672.

[11] Simón L, Goodman J M. How reliable are DFT transition structures? Comparison of GGA, hybrid-meta-GGA and meta-GGA functionals. Organic & biomolecular chemistry, 2011, 9(3): 689-700.

[12] Zeng Z, Chang K C, Kubal J, et al. Stabilization of ultrathin (hydroxy) oxide films on transition metal substrates for electrochemical energy conversion. Nature Energy, 2017, 2(6): 1-9.